INTERNATIONAL JOURNAL FOR NUMERICAL METHODS IN FLUIDS
Int. J. Numer. Meth. Fluids 2001; **36**: 711–742 (DOI: 10.1002/fld.154)

Evaluation of erosion in a two-way coupled fluid–particle system

Yang-Yao Niu*,[1]

Institute of Mechanical and Aerospace Engineering, Chung-Hua University, Hsin-Chu 30067, Taiwan, Republic of China

SUMMARY

In this study, the effects of flow turbulence intensity, temperature, particle sizes and impinging velocity on erosion by particle impact are demonstrated numerically. Underlying turbulent flow on an Eulerian frame is described by the compressible Reynolds averaged Navier–Stokes equations with a RNG k–ε turbulence model. The particle trajectories and particle–wall interactions are evaluated by a Eulerian–Lagrangian approach in a two-way coupling system. An erosion model considering material weight removal from surfaces is used to predict erosive wear. Computational validation against measured data is demonstrated satisfactorily. The analysis of erosion shows that the prevention of erosion is enhanced by increasing the effects of flow temperature and turbulence intensity and reducing particle inertial momentum. Copyright © 2001 John Wiley & Sons, Ltd.

KEY WORDS: erosion; particle–wall collision; turbulence; two-phase flow

1. INTRODUCTION

In the power industry, metallic surface erosion by solid particle impact can substantially shorten the lives of pipelines, heat exchanger systems, and turbomachinery surfaces. In general, erosion prevention depends on the following factors: (i) material properties of solid particle and metallic surface; (ii) flow characteristics of particle and fluid phases. During the past years, the efforts to understand the influences of flow characteristics on erosion have been extensively investigated. The corresponding particle-laden flow motions with erosive wear in industrial applications [1] can be categorized as (1) impingement flows with application to metal cutting which has been studied by Finnie *et al.* [2–6], Tilly [7], Benchaita *et al.* [8,9] and Dosanjh and Humphrey [10]; (2) boundary layer flows occurring in turbomachinery equipment seen in the

* Correspondence to: Department of Mechanical Engineering, Institute of Aeronautics and Astronautics, Chung-Hua University, 30 Tung Shiang, Hsin-Chu 30067, Taiwan, Republic of China.
[1] E-mail: yniu@chu.edu.tw

Received November 1999
Revised February 2000

series of works by Tabakoff *et al.* [11–15]; (3) confined flows applied to pipeline systems performed by many researchers [16–20]; (4) obstructed flows passing over heat exchangers studied in [21–23]. These previous works have demonstrated that flow conditions, such as the particle impacting velocity, particle sizes, flow temperature and turbulence intensity, play important roles in the development of erosion. These previous results have also shown that the erosion depth rate was greater with the higher impacting particle velocities and larger particle sizes. And the relative rate of erosion was found to decrease with the increase of flow turbulence intensity and temperature due to the enhanced axial diffusion [1]. Before predicting erosive wear, numerical modeling of particle-laden turbulent flows is required. There are two different approaches to predict particle dispersion in turbulent carrier flows; one is the Eulerian–Eulerian method, which is widely used in the studies of Tu [19,23]. The other is the Eulerian–Lagrangian method. Because Lagrangian description of the dispersed phase could deliver the physical behaviors of the individual particles in more details, most simulations of erosion reply on Eulerian–Lagrangian approach in one-way (fluid-to-particle) or two-way (fluid to particle and particle to fluid) coupling system. However, the influences of particle–wall interactions on erosion are not included in most of previous works. Humphrey [1] noted that the evaluation of the turbulence on the particle motion was modeled two different ways: deterministic separated flow (DSF) model [8–10,18] and the stochastic separated flow (SSF) model [18,20–22,24]. The SSF model superimposed a random distribution of turbulent fluctuations directly on the calculated mean flow to act as a driving function in the particle equation of motion. In the study of erosion by Schuh *et al.* [18], both DSF and SSF models show that particles with high inertial number ($\lambda > 1$) are slow to respond to changes in fluid velocity. For the particles with low inertial ($\lambda < 1$), the trajectories of particle computed by both models are not identical; It is shown that the particle traces calculated by the DSF model in flow follow the streamline closely. However, SSF model simulates that the particle traces are sensitive to the influences of turbulent fluctuations in flow field. In the study of tube erosion by Fan *et al.* [21,22], the trajectories of the larger particles over 100 μm are found to deviate considerably from the gas streamlines due to the high inertia. Also, particles smaller than 20 μm with low momentum do not impact with the surface of the tube as seen in the results of the DSF model. Based on a DSF model, Naik and Bryden [20] recently indicate that the solid–gas mixtures with small particles have low inter-phase slip velocities and low impact probability with the pipe walls. However, the particles larger than 50 μm cause higher inter-phase slip velocities and increase the impact probability with the pipe walls. It is noted that the larger particles are relatively insensitive to the turbulence effects of fluid phase.

As a result, turbulence-enhanced diffusion of the particle with high inertia can be considered as a consequence of turbulence-enhanced diffusion in the fluid phase. The mean velocity of the fluid flow is taken as a driving force in the particle equation of the motion based on the DSF model and is used to study erosion by particles with high inertia. The influence of turbulent fluctuations on the particle motion is not considered in this study.

Initially, numerical validation is performed on erosion of a metallic plate by solid particles entrained in a liquid jet by Benchaita *et al.* [8], then applied to study erosion in confined flow for a 90° bend [19,25]. Both the particle trajectory equation and an erosion model are computed by a Lagrangian approach. Also, a three-order restitution coefficient function [15,21,22] is also considered to evaluate the particle–wall interaction. Turbulence structures

among the phases of fluid-to-fluid and fluid-to-particle are solved in a two-way coupling system. The effects of turbulence intensity, temperature, particle sizes and impinging velocity on erosion by particle impact are demonstrated and compared with the corresponding validated data.. In numerical approximations, the fluid flow motions are described by a two-dimensional compressible, Reynolds averaged Navier–Stokes solver with a renormalization group theory (RNG) based k–ε turbulence model. As usual, compressible flow codes are often ineffective at low Mach numbers due to the stiffness of the system eigenvalues [26]. In order to reduce the disparities in the eigensystem, the Roe-type approximate Riemann solver [27] incorporating a preconditioning term [26] is used to enhance the convergence and accuracy for solving the low-speed fluid flow phase. For the particulate flow phase, the fourth-order Runge–Kutta method is adopted to solve the Lagrangian trajectory equations and the erosion model.

2. NUMERICAL MODELS

2.1. Continuous phase equations

In this study, the two dimensional Reynolds-averaged Navier–Stokes equations and the kinetic energy and dissipation equations with a preconditioning pseudo time derivative term are expressed in non-dimensional conservative form as

$$\Gamma \frac{\partial Q_v}{\partial \tau} + \frac{\partial Q}{\partial t} + \frac{\partial F}{\partial x} + \frac{\partial G}{\partial y} = \left(\frac{\partial F_v}{\partial x} + \frac{\partial G_v}{\partial y} \right) + S \tag{1}$$

where, $Q_v = [\rho, u, v, h, k, \varepsilon]$ is the primitive variable vector, $Q = [\rho, \rho u, \rho v, E, \rho k, \rho \varepsilon]$ is the conserved variable vector. Both $F = [\rho u, \rho u^2 + p + 2/3\rho k, \rho uv, \rho u(H + 2/3k), \rho uk, \rho u\varepsilon]$ and $G = [\rho v, \rho uv, \rho v^2 + p + 2/3\rho k, \rho v(H + 2/3k), \rho vk, \rho v\varepsilon]$ are the inviscid flux vectors. The viscous flux vectors F_v and G_v are represented as $F_v = [0, \tau_{xx}, \tau_{xy}, R, \alpha\mu_k(\partial k/\partial x), \alpha\mu_\varepsilon(\partial\varepsilon/\partial x)]$ and $G_v = [0, \tau_{xy}, \tau_{yy}, T, \alpha\mu_k(\partial k/\partial y), \alpha\mu_\varepsilon(\partial\varepsilon/\partial y)]$. τ is the pseudo-time and t is the physical time. The variables, ρ, u, v, p, E, H are the fluid density, the x- and y-velocity components, static pressure, total energy and total enthalpy respectively. The turbulent kinetic energy is denoted by k and turbulence dissipation rate is ε. The variables R and S are given by

$$R = u\tau_{xx} + v\tau_{xy} + \chi \frac{1}{Re} \frac{\partial a^2}{\partial x}$$

$$T = u\tau_{xy} + v\tau_{yy} + \chi \frac{1}{Re} \frac{\partial a^2}{\partial y} \tag{2}$$

with $\chi = \mu\alpha(\gamma - 1)^{-1}$. Re and a are the Reynolds number and the speed of sound respectively. Also, the viscous terms involve stress components, τ_{xx}, τ_{xy}, and τ_{yy}. In addition, the preconditioning matrix derived in the works [26] as

$$\Gamma = \begin{bmatrix} 1/\beta & 0 & 0 & 0 & 0 & 0 \\ u/\beta & \rho & 0 & 0 & 0 & 0 \\ v/\beta & 0 & \rho & 0 & 0 & 0 \\ H/\beta & \rho u & \rho v & \rho & 0 & 0 \\ k/\beta & 0 & 0 & 0 & \rho & 0 \\ \varepsilon/\beta & 0 & 0 & 0 & 0 & \rho \end{bmatrix} \tag{3}$$

is used to enhance the convergence rate of the steady state solutions in the low Mach number flow region. To obtain well-conditioned eigenvalues, the scaling factor is taken to be $\beta = u^2 + v^2$.

In the work, the renormalization group theory (RNG)-based k–ε turbulence model suggested by Yakhot and Orszag [28] is employed. In the RNG turbulence transport equation, an inverse Prandtl number α is introduced and can be obtained from the following equation

$$\left|\frac{\alpha - 1.3929}{\alpha_0 - 1.3929}\right|^{0.6321} \left|\frac{\alpha + 2.3929}{\alpha_0 + 2.3929}\right|^{0.3679} = \frac{\nu_l}{\nu_{\text{eff}}} \tag{4}$$

where $\alpha_0 = 1$ and ν_l is the laminar viscosity and the turbulent viscosity $\nu_t = \nu_{\text{eff}} - \nu_l$ and the effective viscosity is given by

$$\nu_{\text{eff}} = \nu_l \left[1 + \sqrt{\frac{C_u}{\nu_l}} \frac{k}{\sqrt{\varepsilon}}\right]^2 \tag{5}$$

The source term S in Equation (1) contains the two-phase momentum exchange terms and the interaction between the particles and the gas phase when the turbulence modulation of the both phase is considered. Its vector form is

$$S = \begin{bmatrix} 0 \\ S_{\text{p},i} \\ S_{\text{p},j} \\ 0 \\ P - \rho\varepsilon + S_k \\ c_1 \dfrac{\varepsilon}{k} - c_2 \dfrac{\rho\varepsilon^2}{k} - R + S_\varepsilon \end{bmatrix} \tag{6}$$

where the production of turbulent energy is based on Boussinesq's approximation is expressed as

$$P = -\rho\overline{u_i'' u_j''} \frac{\partial u_i}{\partial x_j} = \left[\mu_T \left(\frac{\partial u_j}{\partial x_i} + \frac{\partial u_i}{\partial x_j} - \frac{2}{3}(\nabla \cdot \vec{V})\delta_{ij}\right) - \frac{2}{3}\rho k \delta_{ij}\right] \frac{\partial u_i}{\partial x_j} \tag{7}$$

is applied for the Reynolds stresses and the rate of the strain term R is given as

$$R = \frac{C_u \eta^3 (1 - \eta/\eta_0)}{1 + \kappa \eta^3} \frac{\varepsilon^2}{k} \tag{8}$$

where $C_u = 0.09$, $C_1 = 1.42$, $C_2 = 1.68$, $\eta = \sigma k/\varepsilon$, $\eta_0 = 4.38$, $\kappa = 0.012$, $\sigma = \sqrt{2S_{ij}S_{ij}}$ and

$$S_{ij} = \frac{1}{2}\left(\frac{\partial u_i}{\partial x_j} + \frac{\partial u_j}{\partial x_i}\right)$$

Also, the momentum source term in the i-direction as derived in [24] is given as

$$S_{\mathrm{p},i} = \frac{1}{A} \sum_{n=1}^{N} \dot{N} m_{\mathrm{p}} (u_{\mathrm{p,in}} - u_{\mathrm{p,out}} - F_{\mathrm{g},i} \Delta t) \tag{9}$$

where $F_{\mathrm{g},i}$ denotes the gravity force in the i-direction and the summation is carried out over the momentum of all trajectories (N) that traverse a computational cell with the cell area A in a unit time Δt. Also, the effects of particles on the gas turbulence formation [24] are modeled by

$$S_k = -2k(\rho_{\mathrm{p}}/t_{\mathrm{p}})\left[1 - \exp\left(-B_k \frac{t_{\mathrm{p}}}{t_{\mathrm{L}}}\right)\right] \tag{10}$$

and

$$S_\varepsilon = -2\varepsilon(\rho_{\mathrm{p}}/t_{\mathrm{p}})\left[1 - \exp\left(-B_\varepsilon \frac{t_{\mathrm{p}}}{t_{\mathrm{L}}}\right)\right] \tag{11}$$

where the particle response time $t_{\mathrm{p}} = \rho_{\mathrm{s}} d_{\mathrm{p}}^2 / 18 \rho_{\mathrm{g}} \nu$; ρ_{p} the bulk density of the particle phase, ρ_{s} the particle material density, $B_k = 0.09$, $B_\varepsilon = 0.4$ and $t_{\mathrm{L}} = k/\varepsilon$.

2.2. Numerical flux splitting

If only the steady state solution is of interest, the physical–time term can be neglected. The original set of the Navier–Stokes equations is satisfied while the pseudo-time term in Equation (1) is zero. In this study, the inviscid fluxes are evaluated by the Roe type flux-difference splitting [29] with an monotone upstream-centered scheme for the conservation laws (MUSCL) spatial differencing scheme. This approach admits that numerical flux F contains the characteristic information propagating through the domain, with speed and direction according to the eigenvalues of the system. By splitting F into parts, where each part contains the information travelling in a particular direction, i.e. characteristic information, and the split fluxes are differenced according to the directions of the corresponding wave propagation, the interface numerical flux of each cell is then expressed as

$$\hat{F}_{j+1/2} = \frac{1}{2}(F_{j+1/2,\mathrm{R}} + F_{j+1/2,\mathrm{L}}) - \frac{1}{2}(\Gamma^{-1} T |\Lambda| T^{-1})_{j+1/2} \delta Q_{j+1/2} \tag{12}$$

Here δQ is the spatial difference $Q_R - Q_L$. The fluxes $F_R = F(Q_R)$ and $F_L = F(Q_L)$ are computed using the reconstructed solution vectors Q_R and Q_L on the right and left hand sides of the cell face. Here Λ is the diagonal matrix of eigenvalues. The new set of eigenvalues in the ξ direction of the preconditioning governing equations can be obtained from the matrix $\Gamma^{-1}\bar{A}$, where $\bar{A}$ is the Jacobian matrix as

$$\bar{A} = \xi_x A + \xi_y B \tag{13}$$

where T is the modal matrix that diagonalizes $\Gamma^{-1}\bar{A}$, where $\bar{A} = \partial E/\partial Q$ is evaluated using a symmetric average between Q_R and Q_L. The six eigenvalues of the system matrix $\Gamma^{-1}\bar{A}$ are

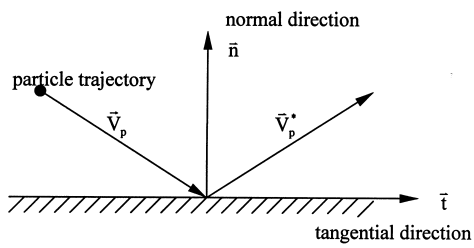

Figure 1. Particle rebounding condition along a solid surface.

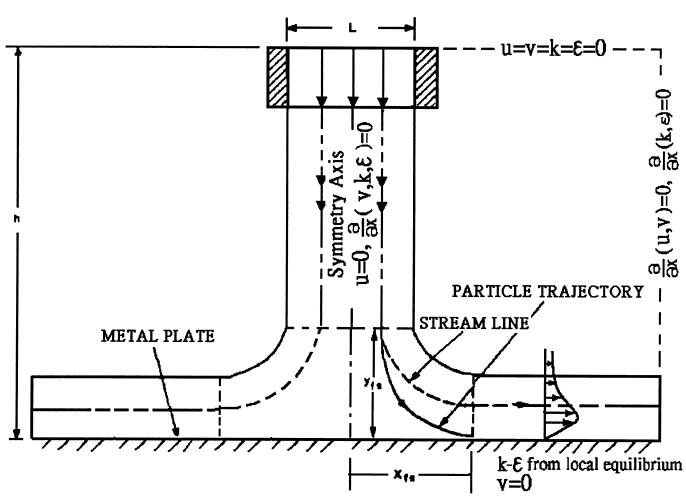

Figure 2. Two-dimensional impinging jet flow.

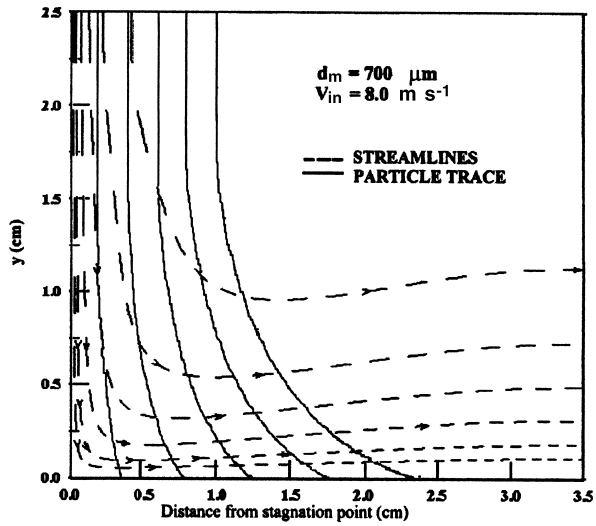

Figure 3. Particle trajectories and fluid streamlines.

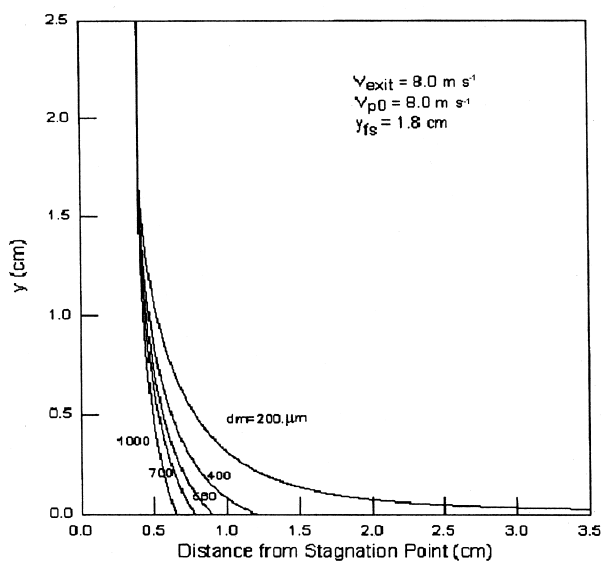

Figure 4. The particle trace of single particle for the different sizes.

$$\lambda(\Gamma^{-1}\bar{A}) = \left(U, U, U, U, \frac{U(1+\beta/a^2) \pm c}{2} \right) \tag{14}$$

where $U = \xi_x u + \xi_y v$ and c is

$$c = \left[U^2 \left(1 - \frac{\beta}{a^2} + 4\beta(\xi_x^2 + \xi_y^2) \right) \right]^{1/2} \tag{15}$$

In the above equations, $\Delta\tau$ is chosen as the local pseudo time step which is determined by the largest eigenvalue of the preconditioning system of governing equations for each grid cell. The implicit LU decomposition method is employed to run the pseudo time iteration. The diffusion terms is evaluated by the standard central differencing scheme.

2.3. Trajectory equations

For computing the dispersed phase in the framework of Lagrangian formulation, with the partial-transformation approach used for the fluid phase, the equations of motion [8,9,24] for each particle can be written as

$$m_p \frac{du_p}{dt} = \frac{C_D}{2} \rho A_p (u - u_p)[(u - u_p)^2 + (v - v_p)^2]^{1/2}$$

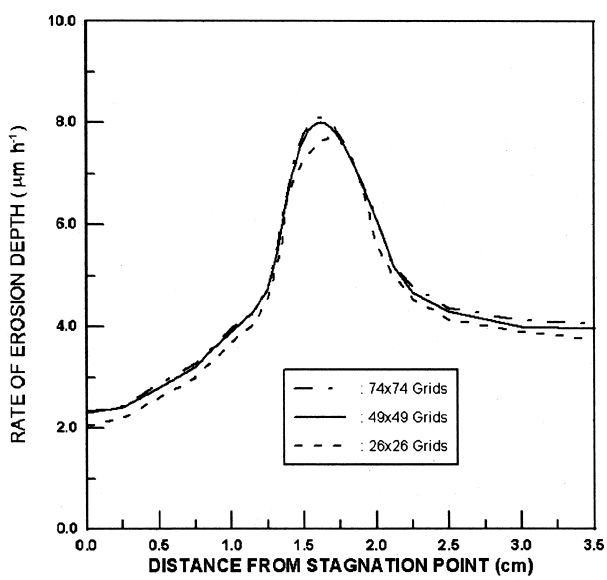

Figure 5. Grid independence study for erosion depth rate ($d_m = 700$ μm, $V_{in} = 7.0$ m s^{-1}, $(\sqrt{K}/U) = 0.01$).

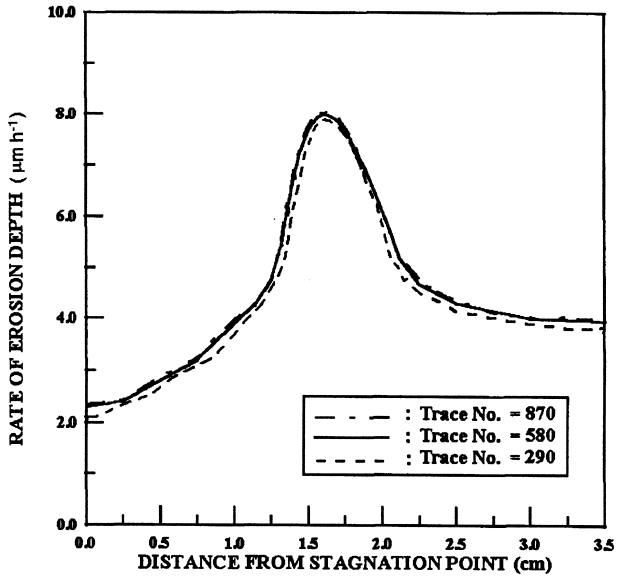

Figure 6. Influence of the particle trace number on the distribution of the erosion depth rate ($d_m = 700$ μm, $V_{in} = 7$ m s^{-1}, $(\sqrt{K}/U) = 2 \times 10^{-4}$, particle trace no. = 290, 580, 870).

$$m_p \frac{dv_p}{dt} = \frac{C_D}{2} \rho A_p (v - v_p)[(u - u_p)^2 + (v - v_p)^2]^{1/2} - m_p(\rho_p - \rho)g \tag{16}$$

where

$$m_p = \frac{\pi}{6} d_m^3 (\rho_p + \rho/2) \tag{17}$$

and m_p represents the abrasive particle mass, A_p the frontal area of the abrasive particle and C_D the drag coefficient. Under the assumption that the case is dilute particle-laden gas flow, the abrasive particle interactions or collisions between particles are neglected; effect of virtual mass, the acceleration-dependent drag, Basset and lift forces including Magnus force, and Saffman forces due to fluid shearing and particle rotation are negligible. For spherical abrasives, the drag coefficient depends solely on the Reynolds number Re_p based on the particle diameter. In the creeping flow regime, Stoke's formula for the drag coefficient is given as

$$C_D = \frac{24}{Re_p} \tag{18}$$

For $Re_p > 10$, the drag coefficient, C_D, can be well correlated by the following formula [24]

$$C_D = \frac{24}{Re_p} + \frac{6}{1+\sqrt{Re_p}} + 0.4 \tag{19}$$

where

$$Re_p = \frac{d_m}{v_l}[(u-u_p)^2 + (v-v_p)^2]^{1/2} \tag{20}$$

Equation (16) can be rewritten by means of the following correction factor [18] as

$$f = \begin{cases} 1 + 0.15Re_p^{0.687} & 0 < Re_p \le 200 \\ 0.914Re_p^{0.282} + 0.0135Re_p & 200 < Re_p \le 2500 \\ 0.0167Re_p & 2500 < Re_p \end{cases} \tag{21}$$

Thus, the equation of motion for an abrasive is

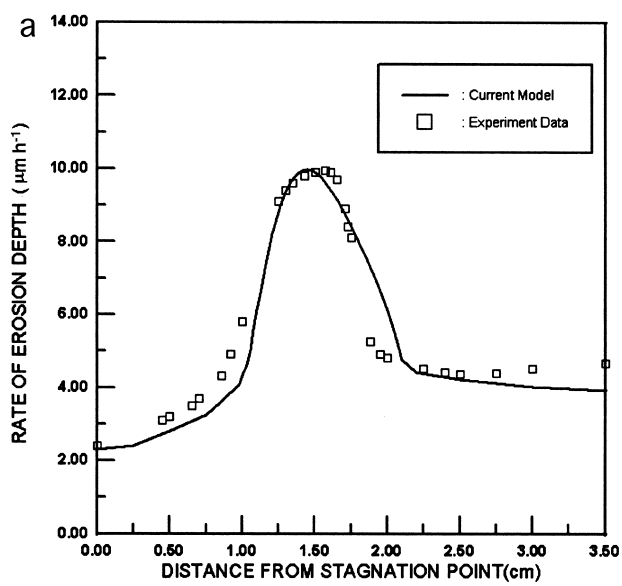

Figure 7. (a) Rate of erosion depth along the metallic plate ($d_m = 700$ μm, $V_{in} = 8.0$ m s^{-1}, $(\sqrt{K}/U) = 0.01$). (b) Rate of erosion depth along the metallic plate ($d_m = 700$ μm, $V_{in} = 7.0$ m s^{-1}, $(\sqrt{K}/U) = 0.01$. (c). Rate of erosion depth along the metallic plate ($d_m = 400$ μm, $V_{in} = 8.0$ m s^{-1}, $(\sqrt{K}/U) = 0.01$).

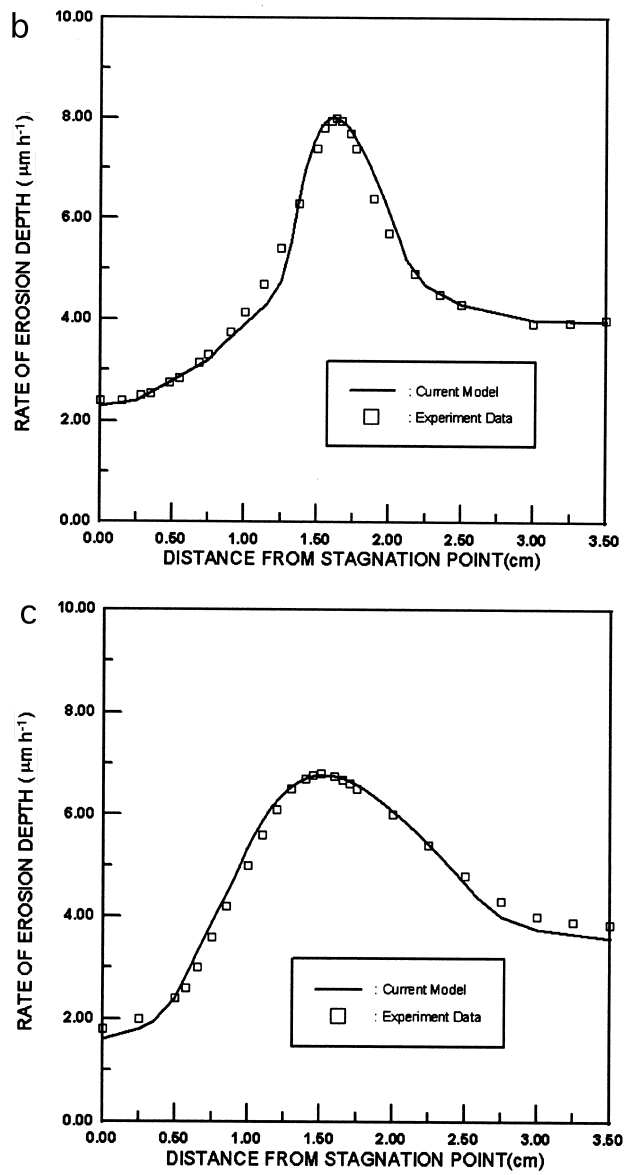

Figure 7 (*Continued*)

$$\frac{\mathrm{d}\vec{U}_\mathrm{p}}{\mathrm{d}t} = g + \frac{f}{\tau}(\vec{U} - \vec{U}_\mathrm{p}) \tag{22}$$

where τ is the particle response time as

$$\tau \equiv \frac{d_\mathrm{m}^2 \rho_\mathrm{p}}{18\mu}$$

and a non-dimensional particle response time or momentum equilibration constant λ is defined to measure the particle inertia momentum

$$\lambda = \frac{\tau U_\mathrm{ref}}{L_\mathrm{ref}}$$

where U_ref and L_ref are the corresponding characteristic velocity and length in the flowfield, respectively. To reduce the computational cost, the particle motion equations are solved by the DSF model [8–10,18] in which the velocities of continuous phase as shown in Equation (16) are expressed by the time-averaged gas velocity obtained in Equation (1). It is assumed that the particle motion is attributed entirely to the mean flow differences between phases due to the

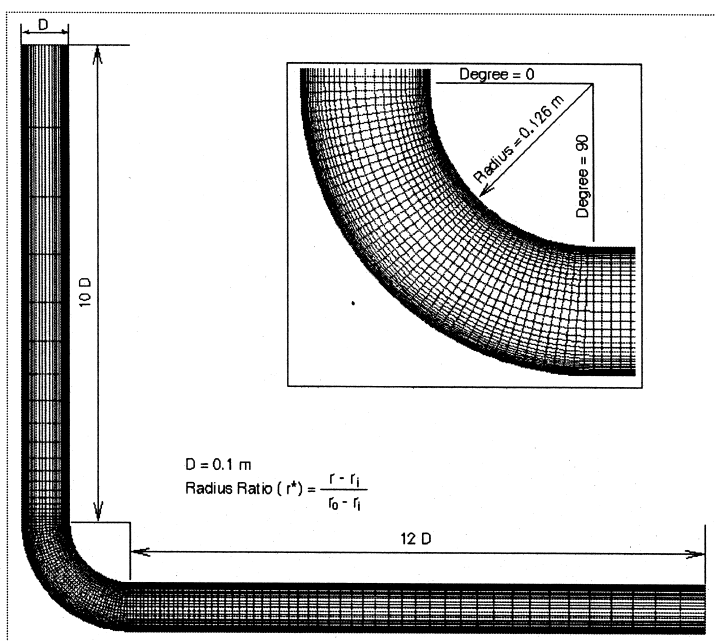

Figure 8. Geometry and computation domain of 120×31 grids for a 90° bend (sketched from Tu and Fletcher [19]).

large particle inertial momentum [20–22]. As a result, the erosion contributed by turbulence-enhanced diffusion of the particle phase is only considered as a consequence of turbulence-enhanced diffusion in the fluid phase. To evaluate the particle trajectory, the equations of motion for a single particle are solved by a fourth-order accurate Runge–Kutta method. It is well known that the Lagrangian formulation in computing the dispersed phase is free of computational meshes, whereas the solution to the continuous fluid phase is based upon the Eulerian finite-volume cell of non-orthogonal grids. However, results of the dispersed phase are often presented in terms of Eulerian grids for easy comparison with experimental measurements. Therefore, the particle locating algorithm of Chen [24] is used to determine fluid properties in the Lagrangian equations due to two-way coupling, also requires knowing the information of a Eulerian cell where a particle stays, and this work has to be carried out at each Lagrangian time step. The independence study of the time step in Equation (22) is shown in the following section.

2.4. Particle rebounding condition

Before proceeding to the surface erosion estimation, the impact location, impact velocity and impact angle of particles on the solid surface need to be determined. This information can be computed from the particle trajectory calculations. However, the determination of particle rebounding conditions after the striking relies on empirical correlations of restitution

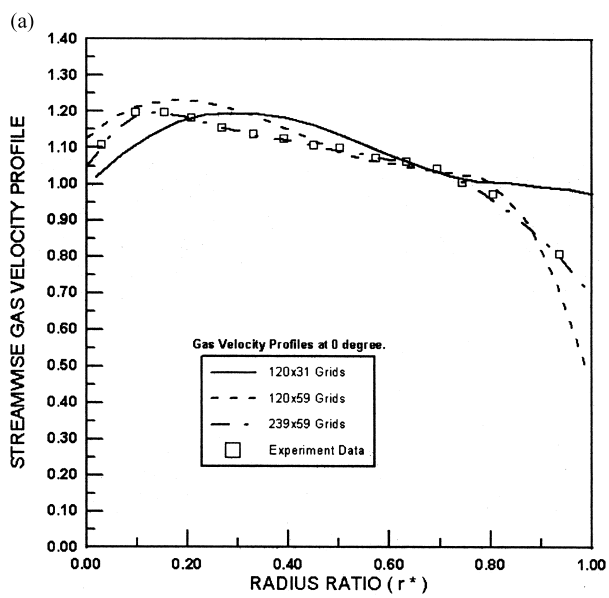

Figure 9. (a) Grid refinement study of gas phase velocity profile distributes at the 0° station of the bend. (b) Grid refinement study of gas phase velocity profile distributes at the 15° station of the bend. (c) Grid refinement study of gas phase velocity profile distributes at the 30° station of the bend.

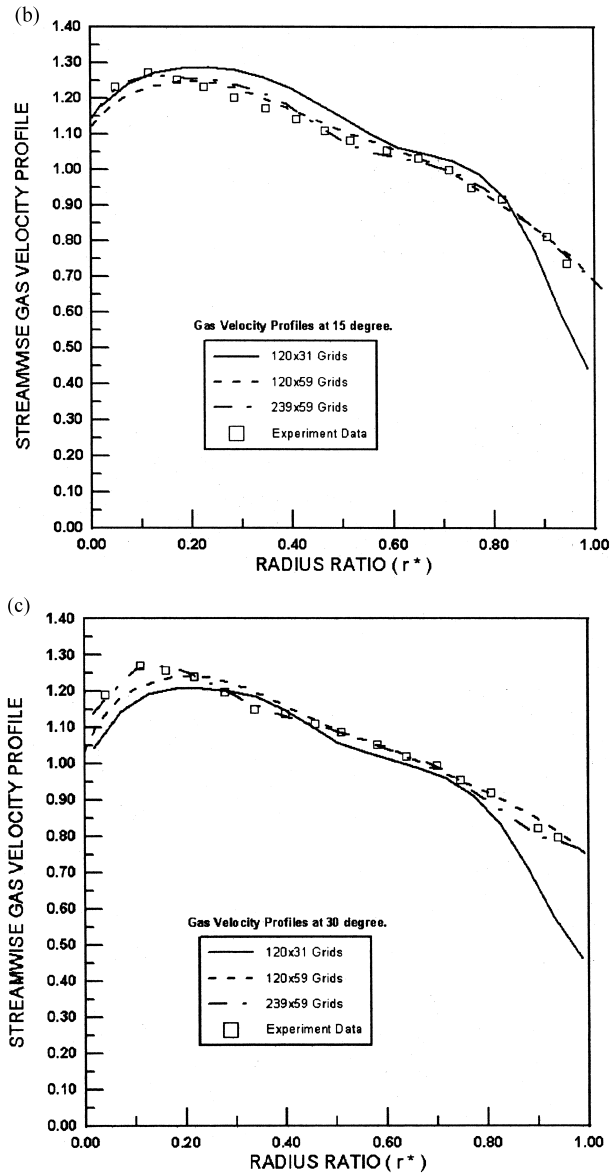

Figure 9 (*Continued*)

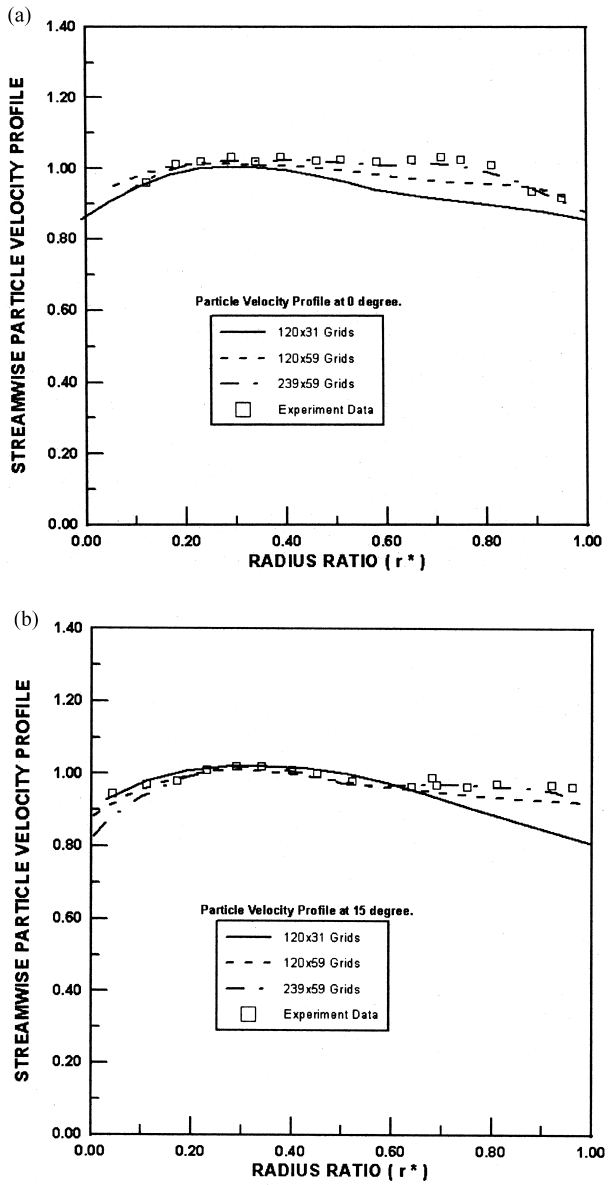

Figure 10. (a) Grid refinement study of particle velocity profiles at the 0° station of the 90° bend. (b) Grid refinement study of particle velocity profiles at the 15° station of the 90° bend. (c) Grid refinement study of particle velocity profiles at the 30° station of the 90° bend.

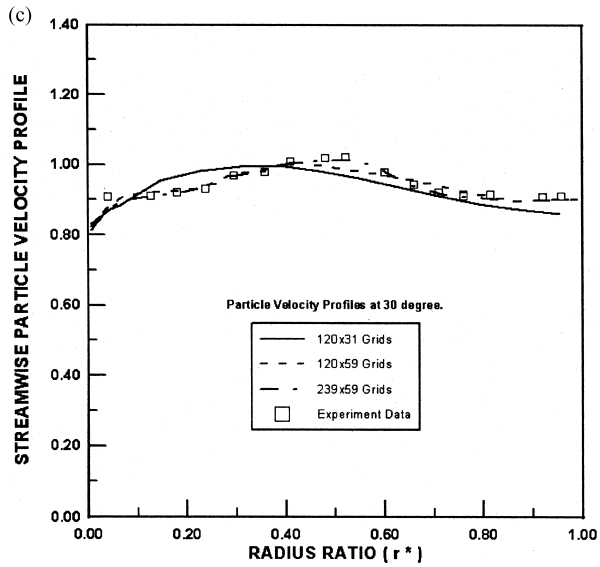

Figure 10 (*Continued*)

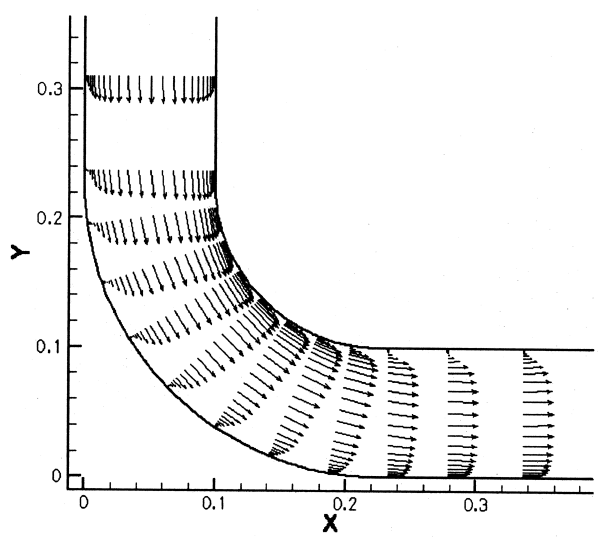

Figure 11. Gas phase velocity vector distribution in the 90° bend.

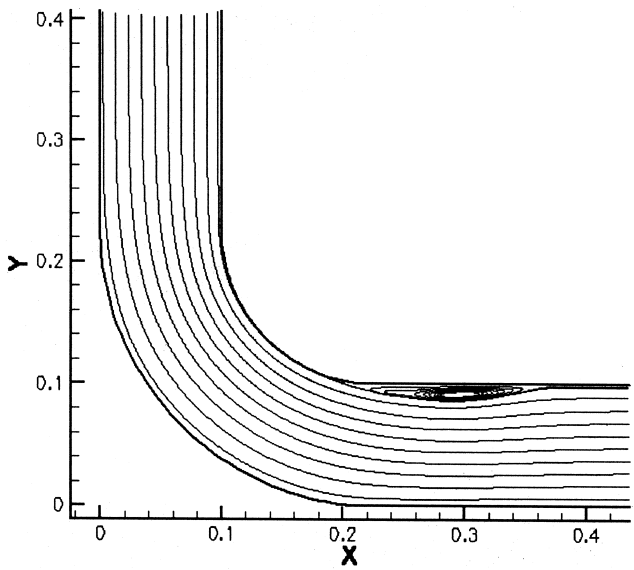

Figure 12. Streamtrace plot for the 90° bend.

parameters in terms of the particle impingement angle and the properties of the ductile metal which have been reported by Tabakoff *et al.* [12]. The particle rebounding conditions are given in the following: as shown in [12,24] like Figure 1, a normal vector $\vec{N}$ to the solid surface can be decided in the process of locating the particle position. A unit vector can be easily obtained by carrying out normalization

$$\vec{n} = \frac{\vec{N}}{|\vec{N}|} \tag{23}$$

To determine the particle velocity after its interaction with the solid wall, its two decompositions must be estimated in the directions normal and tangential to the wall. To this end, the normal component can be computed by

$$\vec{v_{\mathrm{p,n}}} = -|\vec{v_{\mathrm{p}}} \cdot \vec{n}|\vec{n} \tag{24}$$

where $\vec{v_{\mathrm{p}}}$ denotes the particle velocity vector, $\vec{v_{\mathrm{p,n}}}$ its decomposition in the normal direction, and $|\vec{v_{\mathrm{p}}} \cdot \vec{n}|$ the absolute value of the projection of $\vec{v_{\mathrm{p}}}$ onto $\vec{n}$. The tangential component can be determined by

$$\vec{v_{\mathrm{p,t}}} = \vec{v_{\mathrm{p}}} - \vec{v_{\mathrm{p,n}}} \tag{25}$$

The particle velocity after it rebounds from the wall can be determined by

$$\vec{v}^{*}_{\mathrm{p,n}} = -e_{\mathrm{n}}\vec{v}_{\mathrm{p,n}}, \qquad \vec{v}^{*}_{\mathrm{p,t}} = +e_{\mathrm{t}}\vec{v}_{\mathrm{p,t}} \tag{26}$$

where e_{n} and e_{t} are the restitution coefficients for the normal and tangential directions, respectively. The restitution coefficients are expressed as a polynomial function of the impingement angle θ in the following manner

$$\bar{e}_{\mathrm{n}} = 1 - 0.4159\theta - 0.4994\theta^2 - 0.292\theta^3$$

$$\bar{e}_{\mathrm{t}} = 1. - 2.12\theta + 3.0775\theta^2 - 1.1\theta^3 \tag{27}$$

Finally, the particle velocity after interacting with the wall is given by

$$\vec{v}^{*}_{\mathrm{p}} = e_{\mathrm{t}}\vec{v}_{\mathrm{p,t}} - [e_{\mathrm{t}} + e_{\mathrm{n}}]\vec{v}_{\mathrm{p,n}} \tag{28}$$

2.5. Erosion model

Numerical prediction of metallic surface erosion is usually based on the empirical correlation of the given particle-surface material properties associated with the particle impact conditions.

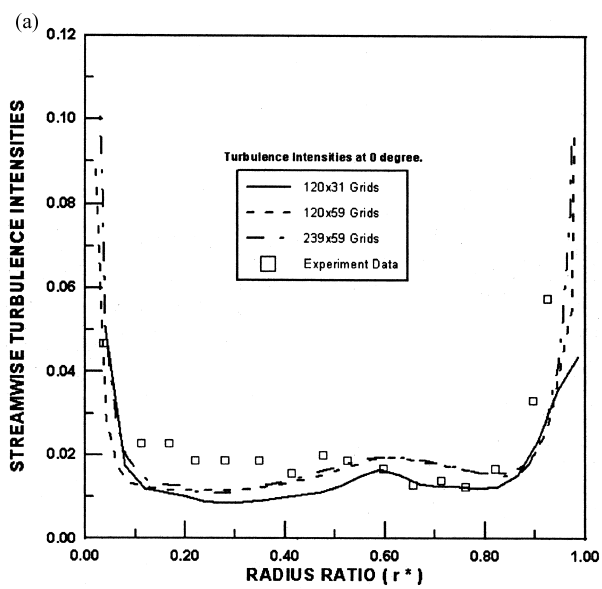

Figure 13. (a) Grid refinement study of streamwise turbulence intensity profiles at the 0° station of the 90° bend. (b) Grid refinement study of streamwise turbulence intensity profiles at the 15° station of the 90° bend. (c) Grid refinement study of streamwise turbulence intensity profiles at the 30° station of the 90° bend.

(b)

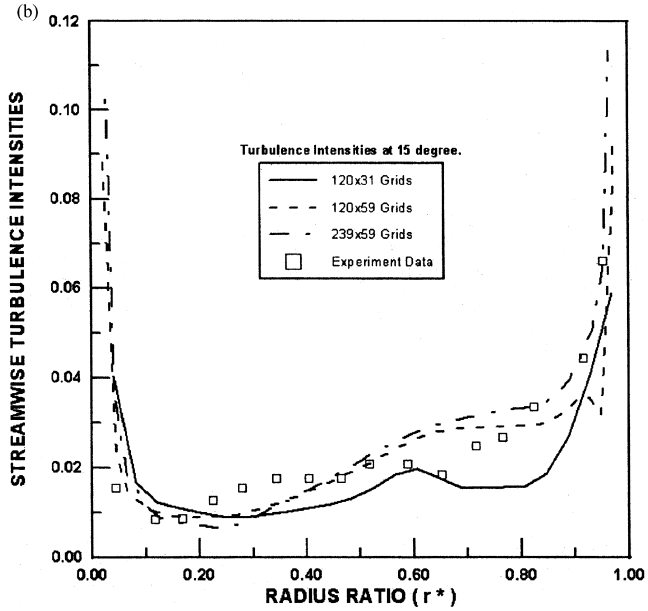

(c)

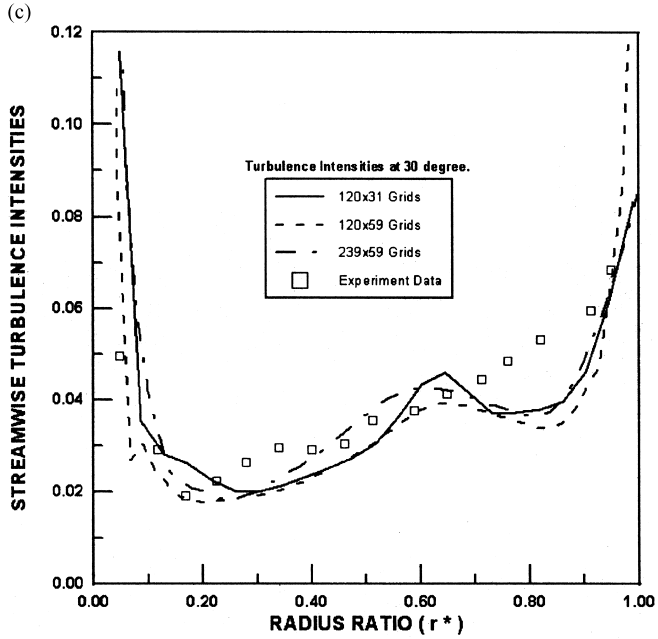

Figure 13 (*Continued*)

The experiment of Tabakoff *et al.* [15] has indicated that the erosion of a specimen was dependent on the particle impingement angles and its impact velocity. The following equation was developed by Tabakoff *et al.* [15] and used by Fan *et al.* [21,22] to predict the erosion of the ductile alloys

$$H = K_1\left[1 + CK\left\{K_{12}\sin\left(\frac{90}{\theta_0}\theta\right)\right\}\right]^2 V_p^2 \cos^2\theta_1(1 - R_t^2) + K_3(V_p \sin\theta)^4 \tag{29}$$

where H is defined as the ratio of the eroded mass of the specimen material to the mass of impinging particles, V_p, θ and θ_0 are the impact velocity, impingement angle and the angle of maximum erosion, respectively. Also, $K_1 = 1.505101 \times 10^{-6}$; $K_{12} = 0.296077$; $K_3 = 5.0 \times 10^{-12}$ are selected as empirical constants for the stainless steel erosion by coal ash particles. In additionn, $R_t = 1 - 0.9916V_p \sin\theta$ and

$$CK = \begin{cases} 1 & \text{for } \theta \le 3\theta_0 \\ 0 & \text{for } \theta > 3\theta_0 \end{cases}$$

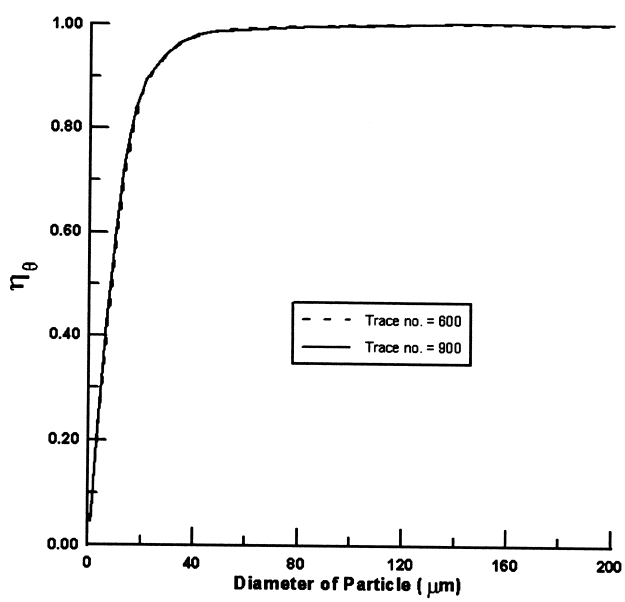

Figure 14. Effect of particle size and inlet particle number on the particle impact frequency on the outer surface of the bend.

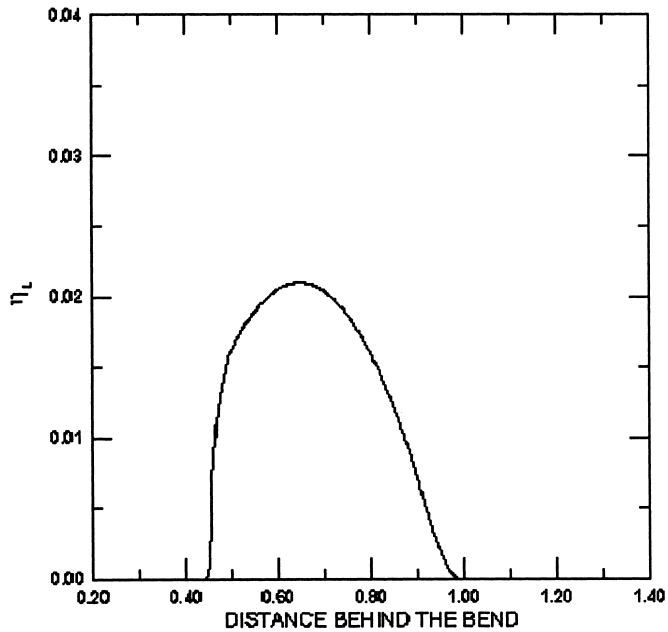

Figure 15. Particle impact frequency on the inner surface behind the bend.

3. NUMERICAL RESULTS

3.1. Impingement jet

Initially, numerical validation of the erosion prediction in the current two-way coupling system is performed for an impingement jet flow of Benchaita *et al.* [8,9]. In the work of Benchaita *et al.*, the potential flow is assumed over the metallic plate. The theoretical predictions of erosion depth rate distributions by Benchaita *et al.* had a large disparity with measured data due to the negligence of viscosity. In order to improve their predictions, the gas turbulence effects and particle–wall interaction are accounted for in the current study using the Eulerian–Lagrangian method. As depicted in Figure 2, a computational domain is based on the nozzle with diameter 2.0 cm, the width of the flat plate 10 cm and the distance from nozzle to the flat plate 5 cm. For simulating two-phase impinging jet flow, the flow conditions used in [9] involve solid concentration $\gamma = 0.32 \times 10^{-2}$, particle material density $\rho_p = 2400$ kg m^{-3}, fluid density $\rho = 1000$ kg m^{-3}. In addition, jet velocities $V_e = 5.5$, 7.0 and 8.0 m s^{-1}, $d_m = 400$ and 700 μm, turbulence intensities $(\sqrt{K}/U) = 0.01$, 0.005 and 0.0025 are chosen, respectively, for the discussion. The grid refinement studies are separately performed on meshes 26×26, 49×49 and 76×76 to verify the calculations. The erosion of model for the sand–water jet flow suggested by Benchaita *et al.* is used to validate our predictions. In this case, the boundary layer, vorticity, and secondary layer effects are neglected as assumed in [9]. First, the

streamlines of fluid flows and trajectories of the particles at the different positions from the nozzle centerline x_f are depicted in Figure 3. Because the buoyancy force is larger than the drag force on the abrasive, the larger particle has a tendency to deviate from the jet flow streamline. In Figure 4, it is found that the particles smaller than 200 μm tend to leave from the plate without the collision. In addition, the impact angle of the particle is shown to be close to the normal angle as the particle size is increased. The grid-independence study with a particle size $d_m = 700$ μm and jet flow velocity 7.0 m s^{-1} is selected for the prediction of the erosion depth rates. Figure 5 demonstrates that the present calculation is grid-independent when the utilized grid points are over 49×49. Thus, the 49×49 meshes are selected for the subsequent computations. Also, based on 49×49 grid points, the independence of particle trace number released at the nozzle exit is studied. Figure 6 shows that using 290 or more particle traces is essential to achieve the accurate profiles of erosion depth rate. Therefore, 290 particles are chosen for release at the nozzle entrance for the following study of erosion.

Figure 7(a)–(c) compare the predicted position of maximum erosion depth and the spreading region for the material removal model with the measured data [9]. It is found that the erosion profile estimated by the current model has better agreement with the experimental data than the theoretical results which are provided in [9], especially on the predicted position of maximum erosion depth. It is seen that the maximum erosion depth is greater for the larger abrasive size, but a larger spread of erosion along the metallic plate is obtained for smaller abrasive. Due to the large ratio of horizontal drag force to vertical drag force, small abrasives

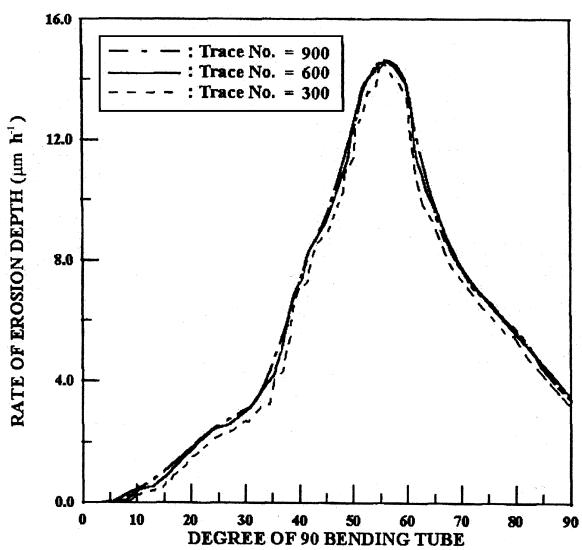

Figure 16. Influence of the particle trace number on the distribution of the erosion depth rate ($d_m = 50$ μm, $V_{in} = 52.19$ m s^{-1}, $(\sqrt{K}/U) = 2 \times 10^{-4}$).

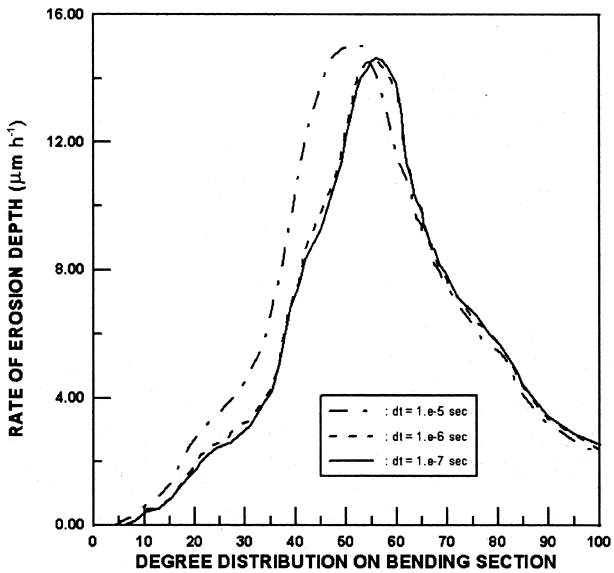

Figure 17. Influence of the particle computation time step on the prediction of the erosion depth rate ($d_m = 50$ μm, $V_{in} = 52.19$ m s^{-1}, $(\sqrt{K}/U) = 0.12$, particle trace no. = 600).

are carried in the main stream far from the stagnation point. On the contrary, the large abrasives have a tendency to hit the metallic plate at positions very close to the stagnation point. Thus, for the larger abrasive, larger erosion rates are obtained in a narrow band around the stagnation point. Meanwhile, a larger spread of erosion (i.e. erosion of a larger surface area of the metallic plates is obtained for smaller abrasive sizes. Besides, erosion at the stagnation point, which was neglected in the theoretical model, is captured by the current model and is in good agreement with experimental profiles. This could explain why all theoretical predictions of erosion dropped after a distance for which all abrasives have impinged on the metallic plate once. However, the influence of abrasive particle bounce back to the plate due to turbulent fluctuations and abrasive–wall interactions have been taken into account by the current approach.

3.2. 90° bend

Subsequently, the capability of analyzing erosion is extended to the case of the turbulent gas–particle flow through a 90° bending tube. The computational domain and grid mesh distribution used is shown in Figure 8. First, numerical comparison with the LDV results of Kliafas and Holt [25] for turbulent gas–solid particle flow in a 90° bend is used to verify the computations. The flow conditions used in [19,25] is assumed for a dilute particle suspended in a gas flow. They are: the bulk velocity is $U_b = 52.19$ m s^{-1} corresponding to the Reynolds number 3.47×10^5; the inlet turbulence intensity of the gas phase is 1 per cent; the particle

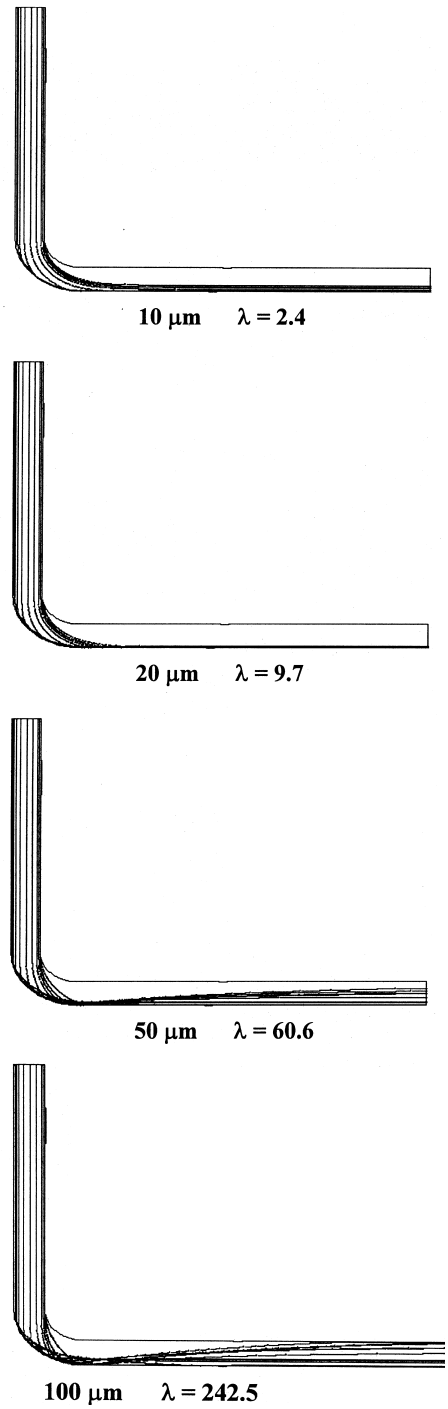

Figure 18. Particle traces of the bend for $V_{in} = 52.19$ m s^{-1}, $(\sqrt{K}/U) = 0.012$.

diameter size 50 μm; the particle material density $\rho_s = 2990$ kg m^{-3}; the inlet particulate bulk density $\rho_{p,in} = 1.8 \times 10^{-4}$ kg m^{-3}. The corresponding particle loading and volumetric ratios are 1.5×10^{-4} and 6×10^{-8}.

The grid independent solutions of mean streamwise velocity profiles carried out for the gas phase and particle phase at the $\theta = 0°$, 15° and 30° stations are shown in Figure 9(a)–(c) and Figure 10(a)–(c). It is seen that the two finest grids have yielded almost identical solutions that are in very good agreement with Kliafas and Holt's measurements. Figures 11 and 12 shows numerical prediction of gas–particulate flow through a 90° bend in terms of velocity vectors and streamtrace distributions. The maximum values of gas velocity profiles are found to displace toward the inner wall, as a result of the favorable streamwise pressure gradient present. It is also found that there is deceleration of the flow near the outer wall due to an adverse pressure gradient on the upper half of the bend. A secondary flow region near the inner wall is clearly observed in the streamtrace plot. Also, the predictions of streamwise turbulence intensity estimated by a RNG k–ε turbulence model, compared with the measurements at the $\theta = 0°$, 15° and 30° stations, are presented in Figure 13(a)–(c). The high turbulence intensity near the two side walls is observed. It is shown that the computed turbulence intensities on fine grids agree with the validated data. It is also seen that the grid-independent solutions are achieved on the grid distributions of 120×59 and 239×59.

To decide the inlet particle number required for solving the particle trajectory equation, the particle–wall frequency, defined in [22] as the ratio of the particle number colliding with the

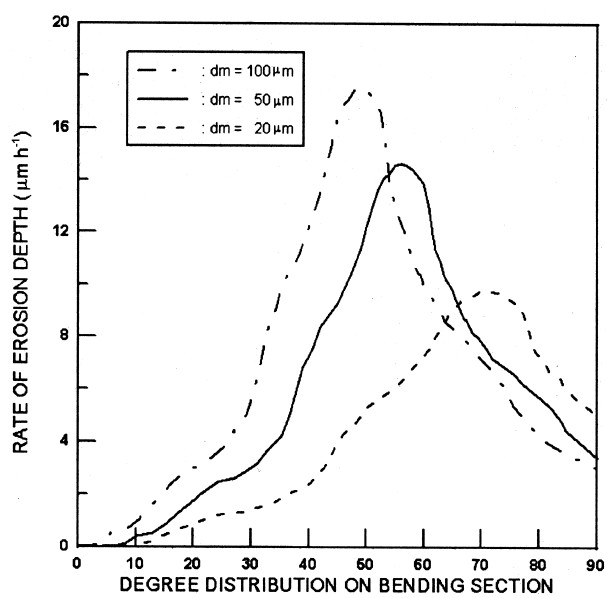

Figure 19. Erosion depth distribution along outer surface of the 90° bend by different particle size ($V_{in} = 52.19$ m s^{-1}, $(\sqrt{K}/U) = 2 \times 10^{-4}$).

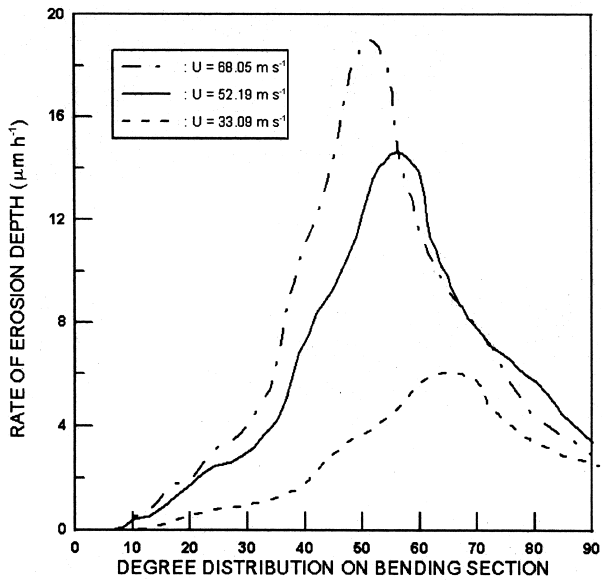

Figure 20. Erosion depth distribution along the outer surface of the 90° bend by different particle inlet velocity ($d_m = 50$ μm, $(\sqrt{K/U}) = 2 \times 10^{-4}$).

wall to the particle number initially released at the inlet, is used. The study of the effect of particle size and number on the particle impact distribution along the walls is performed. Figure 14 shows that an increase in the particle size is associated with higher values of the particle impact frequency for colliding with the outer wall. It is also seen that using 600 and 900 particle traces obtains the same impingement frequency profile distribution. In addition, the impact frequency study demonstrates that the particles smaller than 200 μm scarcely collides with the inner wall. In Figure 15, the impact frequency of the 200 μm particle is shown to be small on the upper surface after the bend section. Therefore, a secondary flow region near the inner wall, as shown in Figure 12, is found not to influence the formation of erosion by particle impact. In Figure 16 it is demonstrated that using 600 or more particle traces in the Lagrangian approach based on 120×59 Eulerian grid cells are essential to achieve a consistent profile of erosion depth rate. Based on 120×59 Eulerian grid cells and assuming 600 particle traces released from the entrance of the bending tube is demonstrated accurate enough for the subsequent simulations of erosion. The influence of the Lagrangian time step is shown in Figure 17 to predict the erosion depth rate. $\Delta t = 1e - 6$ is found accurate enough to perform the particle trajectory calculations.

Here, the particle trajectories of different particle sizes are demonstrated in Figure 18. Different particle sizes of $d_m = 10$, 20, 50 and 100 μm are selected for discussing the influence of particle size. Based on the same inlet flow conditions, the effect of particle size on the trajectory and erosion can be observed by the value of the momentum equilibration constant λ. It is shown that most particles with a momentum equilibration constant $\lambda > 10$ collide with

the outer wall. It is also noted that the effect of particle collision is not significant near the inner wall. So the occurrence of erosion is only considered on the outer wall. In Figure 18 it is also seen that the trajectories of the larger particles with higher inertia momentum (with large λ) deviate considerably from the gas streamline. The particle sizes larger than 20 μm follow gas inlet streamlines until they impact the outer surface, then rebounding and deviating more from the streamlines. In contrast, the particle sizes smaller than 20 μm with low momentum will not collide with the surface as they are entrained in the bulk flow. Of course, the smaller particles may impact the surfaces due to the enhanced inertial momentum such as increasing the particle inlet velocity. The study of the influence on particle momentum and flow pattern caused by inlet velocity will be given in the subsequent sections.

In Figure 19 it is shown that larger particle size causes larger erosion depth rates along the outer wall from curved stations $\theta = 0°–90°$. It is illustrated that the larger particle has higher impinging momentum on the outer solid surface and results in a deeper erosion depth. Besides, the peak of the erosion distribution profile is shown to shift to the downstream as the particle size is reduced. Figure 20 shows numerical estimations of erosion along the outer solid surface by different particle inlet velocities. Initial particle velocities of $V_p = 33.09$, 52.19 and 68.05 m s^{-1} are chosen for the comparison. Due to the higher ratio of inertia force to drag force, the particles have a tendency to hit the plate at positions closer to the upstream as the inlet velocity increases. It is found that the particle impact velocity normal to the outer surface of the bending tube gets stronger, and causes a higher erosion depth rate as the inlet particle velocity increases. For the case of lower jet velocity, Figure 20 also shows that the position of

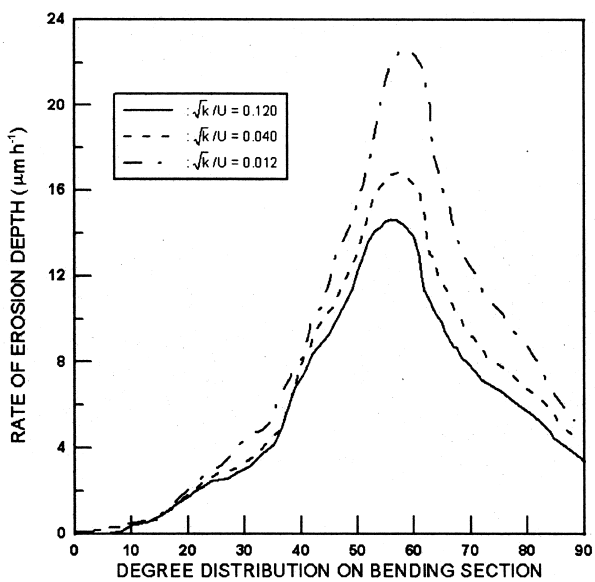

Figure 21. Erosion depth distribution along the outer surface of the 90° bend by different turbulent intensity ($V_{in} = 52.19$ m s^{-1}, $d_m = 50$ μm).

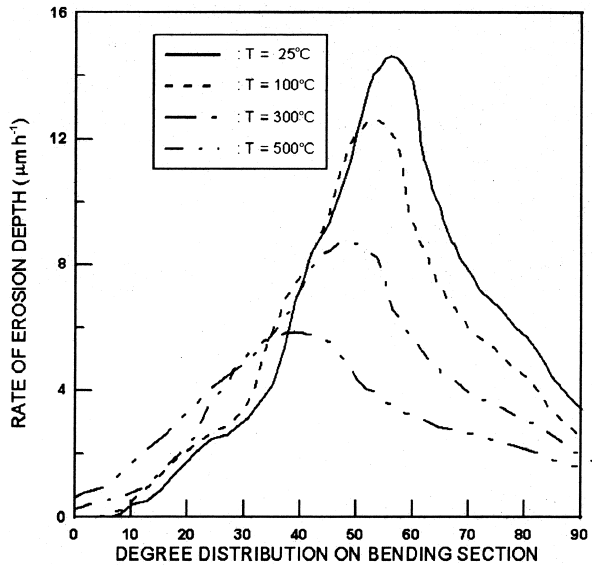

Figure 22. Erosion depth distribution along outer surface of the 90° bend by different flow temperature ($V_{in} = 52.19$ m s^{-1}, $d_m = 50$ μm).

maximum erosion depth is displaced further away from the upstream of the bending flow as the jet velocity is decreased. Furthermore, the effects of the inlet flow turbulence intensity on erosion are investigated. ($\sqrt{K}/U$) = 0.12, 0.04 and 0.012 with the particle size $d_m = 50$ μm and the entrance velocity 52.9 m s^{-1} are chosen for the comparison. In Figure 21, the distributions of erosion caused by different turbulence intensities along tube walls from stations $\theta = 0°$ to 90° are shown. It is seen that the position of the maximum erosion depth moves near the flow downstream and the amount of erosion is reduced as turbulence intensity increases. It is well known that the greater the inlet turbulence intensity, the more momentum mixings lead to larger momentum exchanges between two-phase interactions. The strong inlet turbulence intensity is found to speed up the momentum-spreading rate. Due to the conservation of mass, the axial velocity decreases to balance the larger transverse momentum. So, the particle impact velocity becomes slow; as a result, a smaller erosion depth rate is obtained. Also, a larger transverse momentum reduces the number of particles striking on the wall as the distance from the bending section increases. This could explain why the maximum erosion depth moves closer to the downstream of the pipe flow as the inlet turbulence intensity increases. In addition, the mean erosion distribution profile shifts towards the downstream as the turbulence intensity increases.

The effect of the inlet fluid phase temperature on the erosion based on the same inlet velocity, turbulence intensity and particle size is now discussed. Inlet flow temperatures of 25, 100, 300 and 500°C are selected for the comparison. Heat transfer between phases is not accounted for in the current study. The hotter flows represent the lower flow density and

stronger flow viscosity. Due to conservation of mass, the hotter inlet flows tend to spread the particulate flow faster with the slower axial velocity. So, the number of particles striking the solid wall is reducing, thus weakening the particle impact momentum on the plate. In Figure 22 it is shown that the amount of erosion reduces as the inlet flow temperature increases. The effect of flow temperature can be represented as the increase of the flow viscosity effect.

4. CONCLUSIONS

In this study, numerical prediction of erosion by particle impact has been performed in a two-way coupled system. The inter-phase effects from the dispersed particle phase to the flow phase and the particle–wall collision are accounted for by an Eulerian–Lagrangian approach with a RNG turbulence model. A simple predictive tool based on the modeling of surface material weight loss is utilized to estimate the amount of erosive wear. Numerical validation against measured data is shown to be superior to the previous theoretical work. Computational results reveal that turbulence intensity, particle size, inlet flow velocity and temperature have significant influences on erosion. It is shown that the position of the maximum erosion depth moves closer to the upstream as the inlet turbulence intensity and temperature increase. The amount of erosion becomes less under conditions of stronger inlet turbulence intensity and higher temperature. Also, the position of maximum erosion depth is displaced further away from the upstream as the inlet velocity is decreased. It is shown that erosion occurs while the particles with the inertia number $\lambda > 10$ strike the tube; meanwhile, larger erosion rates are obtained for larger abrasives and the spreading of erosion is obtained for smaller abrasives. In addition, numerical grid-independence is demonstrated in the calculations.

ACKNOWLEDGMENTS

The author wishes to acknowledge the joint project sponsored by the Taiwan Power Company and National Science Council of Taiwan, ROC under Contract NSC-88-TPC-E-216-002.

APPENDIX A. NOMENCLATURE

a	sound speed
A	cell area
C_D	drag coefficient
d_m	mean diameter of particle
e_n, e_t	the restitution coefficients
F, G	the inviscid flux
F_v, G_v	the viscous flux
F_p	the gravity force
H	rate of erosion depth
L_{ref}	the characteristic length

m_p	particle mass
N	particle number
Q	the conserved variable vector
Q_v	the primitive variable vector
R	the rate of the strain term
Re	Reynolds number
Re_p	particle Reynolds number
$S_{p,i}$, $S_{p,j}$	particle collision source term
S_k, S_ε	the source terms of particle effects on fluid turbulence
t	physical time step
t_p	particle response time
T	the eigenvector matrix of the inviscid flux
u, v	x, y component of fluid velocity
u_p, v_p	x, y component of particle velocity
U, V	ξ, η component of fluid velocity
U_p, V_p	ξ, η component of particle velocity
U_{ref}	the characteristic velocity
$\vec{V}$	total velocity vector of fluid
$\vec{V}_p$	total velocity vector of particle
x, y	Cartesian coordinates
x_f, y_f	abscissa of the position of impact in the x, y direction (Figure 2)

Greek letters

α	Prandtl number
β	scaling factor in the preconditioning matrix
ε	turbulent dissipation rate
γ	specific heat ratio
η_L	impact frequency along the inner wall
η_θ	impact frequency along the outer wall
κ	turbulent kinetic energy
λ	particle inertial momentum Λ
ν	fluid dynamic viscosity
ν_{eff}	effective viscosity
ν_t	turbulent viscosity
ρ	fluid density
ρ_p	particle density
τ	Lagrangian time step
τ_{xx}, τ_{yy}, τ_{xy}	shear stress components
θ	particle impact angle
θ_0	angle of maximum erosion
Γ	pre-conditioning matrix
Λ	the eigenvalue matrix of the inviscid flux

Subscripts

$i+1/2, j+1/2,$ etc.	cell interfaces
L	left state of cell interface
R	right state of cell interface
n	normal direction
t	tangential direction

Superscripts

*	after impact solid wall

REFERENCES

1. Humphrey JAC. Fundamentals of fluid motion in erosion by solid particle impact. *International Journal of Heat and Fluid Flow* 1990; **11**(3): 170–194.
2. Finnie I. An experimental study of erosion. *Proceedings of the Society of Experimental Stress Analysis* 1959; **17**(2): 65–70.
3. Finnie I, Wolak J, Kabil Y. Erosion of metal by solid particles. *Journal of Materials* 1959; **2**(3): 65–70.
4. Finnie I. Erosion by solid particles in a fluid stream. In *Symposium on Erosion and Cavitation*, *ASTM Special Techical Publication 307*. ASTM: Philadelphia, PA, 1962; 70–82.
5. Finnie I. Some observations on the erosion of ductile metals. *Wear* 1972; **19**: 81–90.
6. Finnie I, Levy A, McFadden DH. Fundamental mechanisms of the erosive wear of ductile metals by solid particles. In *Erosion: Prevention and Useful Applications*, *ASTM Special Technical Publication 664*, Alder WF (ed.). ASTM: Philadelphia, PA, 1979; 36–58.
7. Tilly GP. Erosion caused by the impact of solid particles. *Treatise on Material Science Technology* 1979; **13**: 287–319.
8. Benchaita MT. Erosion of metallic pipe by solid particles entrained in a liquid. PhD thesis in Mechanical Engineering, Massachusetts Institute of Technology, Cambridge, MA, 1980; 87–98.
9. Benchaita MT, Griffith P, Rabinowicz E. Erosion of a metallic plate by solid particles entrained in a liquid jet. *Journal of Engineering and Industry* 1983; **105**: 215–222.
10. Dosanjh S, Humprey JAC. The influence of erosion by a particle-laden fluid jet. *Wear* 1985; **102**: 309–330.
11. Tabakoff W, Hussein MF. Effect of suspended solid particles on the properties in cascade flow. *AIAA Journal* 1971; **9**: 1514–1519.
12. Hussein MF, Tabakoff W. Erosion prediction in turbomachinery resulting from environmental solid particles. *Journal of Aircraft* 1975; **12**: 471–478.
13. Grant G, Tabakoff W. Erosion prediction in turbomachinery resulting from environmental solid particles. *Journal of Aircraft* 1975; **12**: 471–478.
14. Tabakoff W, Hosny W, Hamed A. A effect of suspended solid particles on the turbine performance. *Journal of Engineering for Power* 1976; **98**: 47–52.
15. Tabakoff W, Kotwal R, Hamed A. Erosion study of different material by coal ash particles. *Wear* 1979; **52**: 161–170.
16. Pourahmadi F, Humphrey JAC. Modeling solid–fluid turbulent flows with application to predicting erosive wear. *Physicochemical Hydrodynamics* 1983; **4**(3): 191–219.
17. Blanchard DJ, Griffith P, Rabinowicz E. Erosion of a pipe bend by solid particles entrained in water. *Journal of Engineering and Industry* 1984; **106**: 213–217.
18. Schuh MJ, Schuler CA, Humphrey JAC. Numerical calculation of particle-laden gas flows past tubes. *AIChE Journal* 1989; **35**(3): 466–480.
19. Tu JY, Fletcher CAJ. Numerical computation of turbulent gas–solid particle flow in 90° bend. *AIChE Journal* 1994; **41**: 2187–2196.
20. Naik S, Bryden IG. Prediction of turbulent gas–solid flow in curved ducts using the Eulerian–Lagrangian method. *International Journal for Numerical Methods in Fluids* 1999; **31**: 579–600.
21. Fan J, Zhou D, Zeng K, Cen K. Numerical and experimental study of finned tube erosion protection methods. *Wear* 1991; **142**: 171–184.

22. Fan J, Zhou D, Jung J, Cen K. Numerical simulation of tube erosion by particle impaction. *Wear* 1992; **152**: 1–19.
23. Tu JY, Fletcher CAJ. Eulerian modeling of dilute particle-laden gas flows past tube. *Computational Fluid Dynamics Journal* 1996; **5**: 45–70.
24. Chen XQ, Pereira JCF. Computational modeling of dilute gas-particle flows in an ultrasonic gas flowmeter. *Flow Measurement Instrumentation* 1997; **8**: 167–182.
25. Kliafas Y, Holt M. LDV measurements of a turbulent air–solid two-phase flow in a 90-degree bend. *Experimental Fluids* 1987; **5**: 73.
26. Shuen JS, Chen KH, Choi Y. A coupled implicit method for chemical non-equilibrium flows at all speeds. *Journal of Computational Physics* 1993; **106**: 306–318.
27. Weiss JM, Maruszewski JP, Smith WA. Implicit solution of preconditioned Navier–Stokes equations using algebraic multigrid. *AIAA Journal* 1999; **37**: 29–36.
28. Yakhot V, Orszag S. A renormalization group analysis of turbulence. *Journal of Science and Computing* 1986; **1**: 3–51.
29. Van Leer B. Towards the ultimate conservation difference scheme: V. A second-order sequel to Godunov's method. *Journal of Computational Physics* 1979; **54**: 194–201.

